

Atomic-scale observation of strain-induced local amorphization in face-centered cubic metals

Zhanxin Wang^a, Nianke Chen^b, Xianbin Li^b, Jiao Teng^c, Yizhong Guo^a, Libo Fu^a, Zihao Zhang^a, Evan Ma^{d,*}, Lihua Wang^{a,*}, Ze Zhang^{a,e}, Xiaodong Han^{a,*}

^a Institute of Microstructure and Properties of Advanced Materials, Beijing University of Technology, Beijing, China

^b State Key Laboratory of Integrated Optoelectronics, College of Electronic Science and Engineering, Jilin University, Changchun 130012, China

^c Department of Material Physics and Chemistry, University of Science and Technology Beijing, Beijing 100083, China

^d Center for Alloy Innovation and Design (CAID), State Key Laboratory for Mechanical Behavior of Materials, Xi'an Jiaotong University, Xi'an 710049, China

^e Department of Materials Science, Zhejiang University, Hangzhou 310008, China

ARTICLE INFO

Article history:

Received 13 December 2021

Revised 14 January 2022

Accepted 19 January 2022

Keywords:

Transmission electron microscopy (TEM)

Metallic glass

Dislocation

Phase transformations

Strain-induced amorphization

ABSTRACT

The formation of metallic glass through melt processing proves to be the most challenging for pure monatomic face-centered cubic (FCC) metals. Though it has long been conjectured that amorphous monatomic metals can be generated through deforming a solid at room temperature, there is rarely direct evidence to prove that is indeed the case. In this study, mechanical loading was applied to nanometer-sized crystals inside an aberration-corrected transmission electron microscopy, and atomic-scale *in situ* evidence is provided of strain-induced amorphization in Pt and Ni near room temperature. The loading was applied in such a way that the stress state is complicated, and the strain distribution is non-uniform, restricting dislocation activities in accommodating the imposed strain. The local lattice distortion is then rendered so large and the associated strain energy is so high that the crystal collapses into the amorphous state. As such, even elemental FCC metals can be forced to become amorphous.

© 2022 Acta Materialia Inc. Published by Elsevier Ltd. All rights reserved.

Since the discovery of metallic glasses (MG) in the 1960s [1], many different types of MGs [2–4] have been obtained from liquids, using fast cooling and rapid solidification such as melt spinning [2], copper mold casting [3], liquid splat-quenching [5], and pulsed laser quenching [6]. While most MG formers are alloys containing two or more elements [2,7], recently monatomic MGs have been achieved through superfast quenching of molten elemental metals, which would otherwise crystallize into body-centered cubic (BCC) structures [8]. However, it has not been possible to retain the amorphous state through the melt-quench route for pure metals that crystallize into FCC structures [8–10]. One naturally wonders if solid-state routes can access the amorphous state for monatomic FCC metals. Circumstantial evidence is available that this may be possible through the accumulation of a high density of dislocations [11–14] in severe deformation, e.g., in some edge regions on fracture surfaces examined postmortem. It has been argued that the amorphization originated from the exceptionally high dislocation density in a small region, where the local en-

ergy density has been raised to above that of the amorphous state. However, there is another possible mechanism: at ambient pressure, the amorphous state can be reached when the lattice strain in the crystal exceeds a critical level to trigger elastic instability [7].

In this study, we demonstrate local amorphization in pure Pt and Ni, observed inside an aberration-corrected (Cs-corrected) TEM, using our home-made *in situ* deformation device [15–17]. We provide atomic-scale evidence that the deformation can indeed lead to crystal-amorphous transition. Our results show that the crystal-amorphous transition is mainly driven by large lattice distortion, which is different from previous studies that suggested that amorphization is induced solely from the accumulation of a high density of dislocations [11–14].

In situ tensile experiments on Pt nanocrystals were conducted using a specially designed double-tilt deformation device in an FEI TITAN G2 (300 kV). First, a Pt nanocrystalline thin film with a thickness of ~25 nm was deposited by means of magnetron sputtering onto a NaCl crystal substrate. Under an optical microscope, this thin film with NaCl substrate, was attached to a bimetallic extensor using an epoxy resin. After washing away the NaCl substrate with water, the Pt thin film became free-standing, which remained on the bimetallic extensor.

* Corresponding authors.

E-mail addresses: maen@xjtu.edu.cn (E. Ma), wlh@bjut.edu.cn (L. Wang), xdhan@bjut.edu.cn (X. Han).

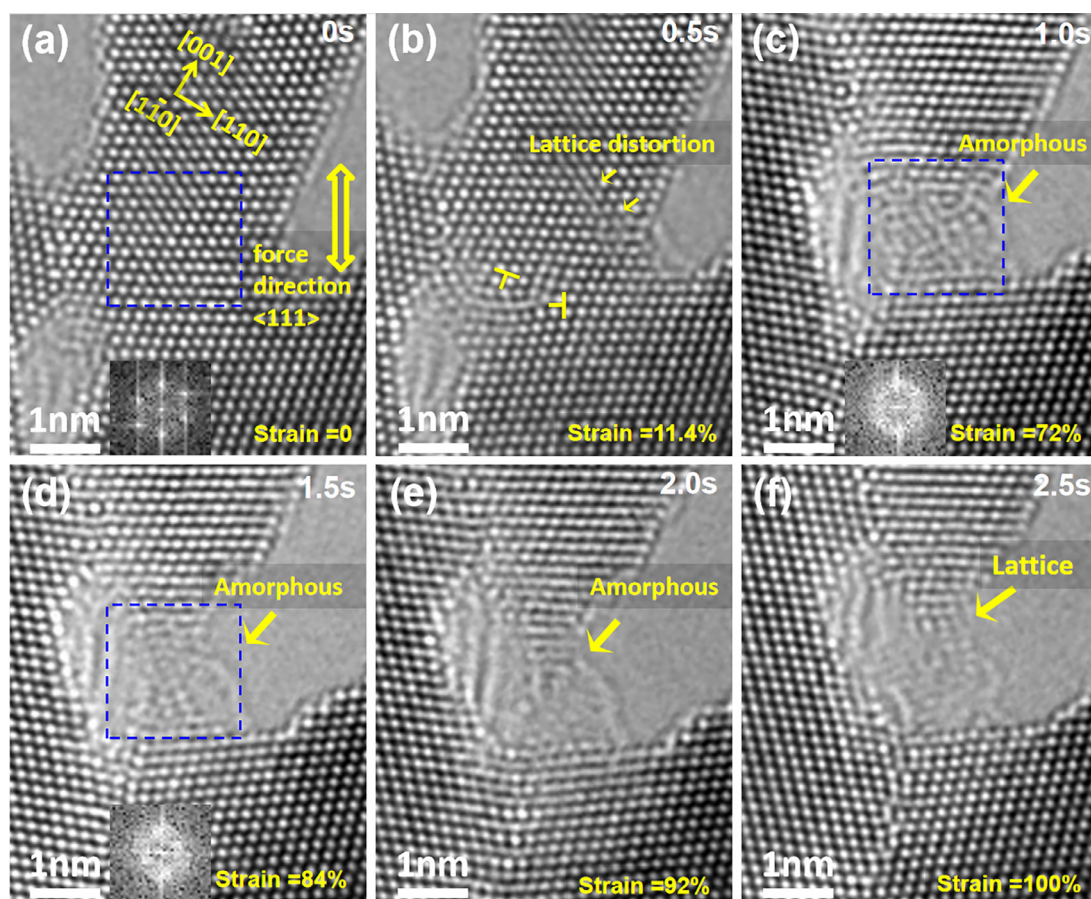


Fig. 1. The Cs-corrected HRTEM images show the atomic-scale observation of strain-induced crystal-amorphous transition in a Pt crystal near room temperature. (a) A perfect lattice at low strain. (b) Lattice distortion at local strain of $\sim 11.4\%$, as indicated by the yellow arrows. (c) With increased straining, the distortion of the lattice became more severe and spread to nearby regions, followed by crystal-amorphous transition. (d–f) The amorphous phase began to re-order back into crystal phase at room temperature. (For interpretation of the references to colour in this figure legend, the reader is referred to the web version of this article.)

The thin film was then further thinned with the Fischione 1040 NanoMill. A high density of pores and nanocrystalline Pt grains were observed in the thin film. Finally, the whole device, together with the as-prepared sample were transferred onto a Gatan double tilt TEM heating holder. During the tensile experiments, a temperature controller was used to control the bimetallic extensor that exerts a tensile force on the Pt nanocrystals due to thermal expansion of the prong holders with increasing temperature (the temperature during experiments was always $< 50\text{ }^\circ\text{C}$), generating a strain rate of $\sim 6 \times 10^{-3}/\text{s}$.

Fig. 1 presents a series of $\langle 110 \rangle$ Cs-corrected high-resolution transmission electron microscopy (HRTEM) images, showing the *in situ* atomic-scale observation of crystal-amorphous transition in a Pt nanocrystal. Fig. 1(a) displays the Cs-corrected HRTEM images of the nanocrystal captured before the deformation. The nanocrystal has a width of $\sim 3\text{ nm}$, and neither dislocation nor stacking fault was observed in the initial nanowire (NW), i.e., the NW was defect-free. The lattice image exhibited the periodic parallelogram-shape, consistent with the FCC structure.

The measured spacings between the lattice planes are 0.228 nm , which matches well with that of the $\{111\}$ plane of FCC Pt viewed along the $\langle 110 \rangle$ zone axis ($a = b = c = 0.393\text{ nm}$). The FCC structure was confirmed by the fast Fourier transform (FFT) image of the dark blue framed region. From Fig. 1(a), the nanocrystal can be seen with its longitudinal axis along the $\langle 001 \rangle$ direction and its left side bounded by the grain boundary (GB). As indicated by the arrow, the loading direction was along the $\langle 111 \rangle$ direction. This special geometry, combined with non-longitudinal di-

rection loading is expected to lead to a complicated stress/strain state in some regions of the nanocrystal. Fig. 1(b) shows the atomic-scale structure of the nanocrystal just before the crystal-amorphous transition, where two full dislocations, marked by “T”, were observed. These two dislocations were on different slip systems and very close to each other. This configuration can efficiently obstruct the further motion of these two dislocations and lead to high stress concentrations.

In addition, local lattice distortion was also clearly detected, as indicated by the yellow arrows. This implies that the nanocrystal sustained high strain/stress before the crystal-amorphous transition. With continued loading, the crystal-amorphous transition occurred across a region of the nanocrystal, as shown in Fig. 1(c). The lattice of the nanocrystal was disordered there, losing all the periodical feature. This was further confirmed by the FFT image of the dark blue framed region, in which the FFT exhibited an amorphous halo feature. This *in situ* observation provides direct evidence that the deformation can indeed trigger the crystal-amorphous transition at near room temperature. Interestingly, upon further loading, as can be seen from Fig. 1(d) and (e), the amorphous lattice underwent a dynamic recovery process during which part of the disordered lattice transformed back into the regular FCC lattice. In other words, the dynamic recovery after the release of local strain/stress allowed the high-energy disordered Pt to back-transform to the ground state FCC-ordered Pt.

Fig. 2(a) and (b) show enlarged Cs-corrected HRTEM images that correspond to Fig. 1(b) and (c), respectively. As indicated by

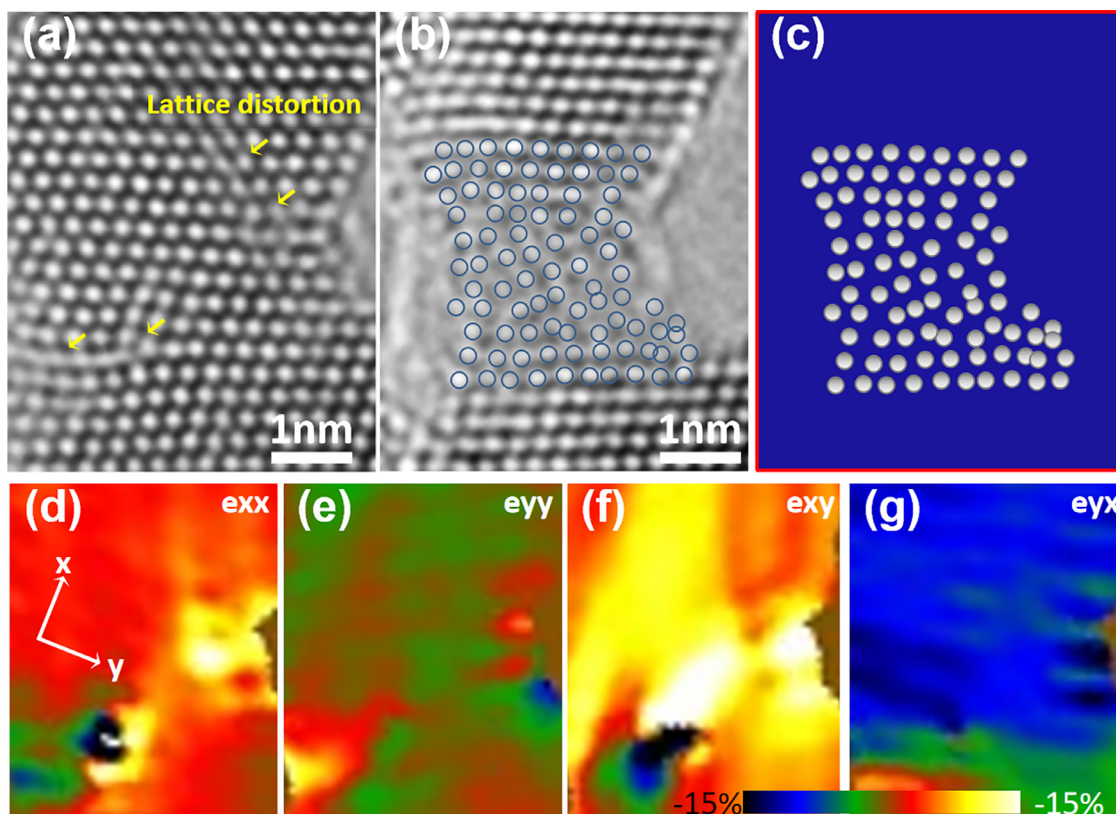


Fig. 2. (a) Enlarged Cs-corrected HRTEM images showing the highly distorted lattice before the crystal-amorphous transition in Pt crystal at room temperature. (b) The lattice distortion became more severe and spread-out, leading to crystal-amorphous transition. (c) Atomic model derived from the actual lattice positions of (b) indicating the presence of an amorphous region. (d–g) Strain maps corresponding to (a).

yellow arrows in Fig. 2(a), some of the lattices were highly distorted before the onset of amorphization. As shown in Fig. 2(b), with continued loading, the periodical FCC lattice at the notch tip exhibited a disordered feature. The blue circles mark the atoms in the crystal-amorphous transition region. Fig. 2(c) shows the atomic model derived from the atomic positions in Fig. 2(b), indicating the emergence of an amorphous region. To reveal the local strain/stress distribution, the geometrical phase analysis (GPA) [18,19] was used to quantify the local lattice strain of the nanocrystal right before the crystal-amorphous transition. Fig. 2(d) to (g) show the strain maps corresponding to Fig. 2(a), with the color variation from dark blue to bright yellow, corresponding to the elastic strain from -0.15 (compressive) to 0.15 (tensile). From Fig. 2(d) to (f), most of the regions show large and complicated non-uniform tensile/shear strain [20]. The sharp contrast in the strain maps corresponds to the highly distorted lattice noted by the yellow arrows in Fig. 2(a). These strain maps provide the direct evidence that high strain/stress concentration, combined with complicated strain distribution, can trigger the crystal-amorphous transition. The reason for amorphization in a severely constrained crystal will be discussed later.

Based on the above results, it can be inferred that amorphization could also happen in nanowires under bending deformation. This was directly observed in a severely bent Ni NW, as shown in Fig. 3. Fig. 3(a) and (b) display two low-magnification TEM images showing the *in-situ* observation of increased bending deformation in the Ni NW. As can be seen from Fig. 3(b), very high bending strain occurred predominantly within a local region of the NW, forming a plastic hinge. Crystal-amorphous transition was observed in the region of the plastic hinge. Fig. 3(c) shows a HRTEM image that corresponds to the red framed region of Fig. 3(b). The lattice in the hinge region was highly disordered, while the lattice

away from the hinge region exhibited a periodical feature. Fig. 3(d) to (f) provide three HRTEM images, showing the crystal-amorphous transition mechanism. Fig. 3(d) presents a typical HRTEM image before the crystal-amorphous transition in the bent NW. At this stage, a high density of full dislocations was distributed in the NW. In this local region, the lattice strain was non-uniform. Upon further bending, the original parallelogram-shaped lattice became highly distorted, as shown in Fig. 3(e). Due to this large lattice strain, this local region was amorphized upon continued bending. That is, the highly distorted lattice became disordered, through a crystal-amorphous transition. This large lattice distortion appears to be the precursor of the collapse of the crystal into an amorphous state.

The *in-situ* HRTEM images show that there is little carbon contamination before and after deformation, the surface of Pt is always clear and clean. In addition, the *in-situ* observation also shows that the amorphous region can be reverted back to FCC, which suggests that the observed crystal-amorphous transition does not come from carbon contamination. We also examined the C-Pt and O-Pt binary phase diagram, in which PtC_x and PtO_x cannot be generated even at high temperature. Thus, the observed amorphous Pt does not result from oxidation. In these experiments, the measured local strain rate is $< 1 \times 10^1/s$, far below that in shock loading, therefore, disqualifying the strain rate as the dominant reason for the observed crystal-amorphous transition.

In summary, based on *in situ* deformation experiments, it has been demonstrated that heavy straining of a crystal can generate local amorphous regions in pure FCC metals. This was achieved under complicated stress states and non-uniform strain distribution, which severely constrains some local regions. In these confined volumes, dislocations do not glide easily, e.g., by slipping through the crystal, to accommodate the imposed plastic strain. The lo-

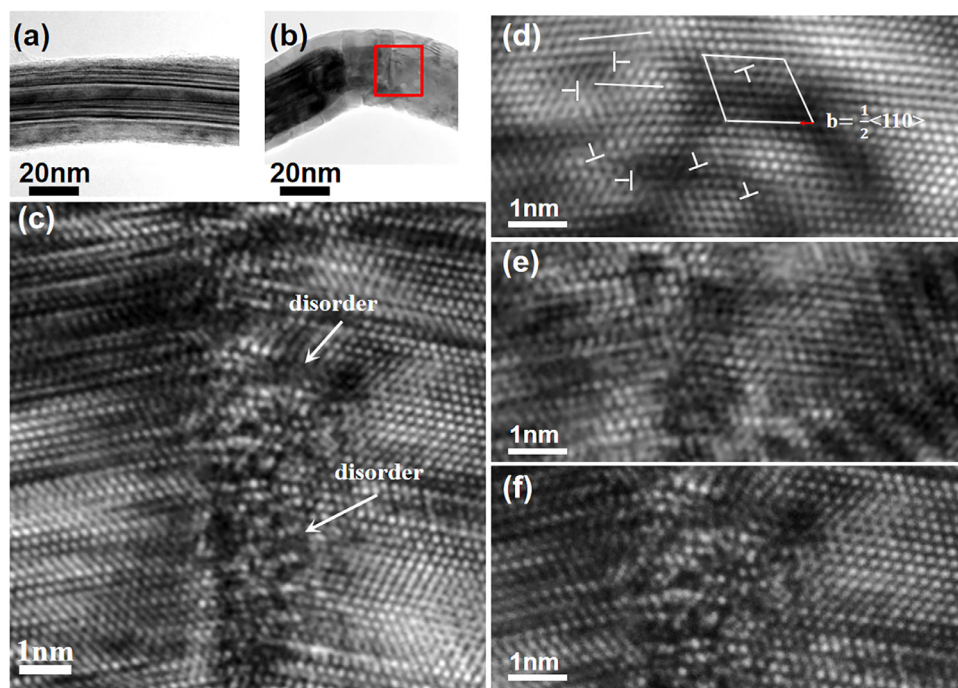


Fig. 3. *In situ* atomic-scale observation of crystal-amorphous transition, driven by bending deformation in a Ni NW. (a and b) Low-magnification TEM images showing that bending induced the formation of a plastic hinge. (c) A representative HRTEM image showing the amorphous feature in the hinge region. (d) HRTEM image captured before the crystal-amorphous transition, a high density of full dislocations was randomly distributed (marked by the symbol T) in the NW. (e) The increasing load led to the original parallelogram-shaped lattice becoming highly distorted. (f) The lattice collapsed, and disordering occurred with further bending.

cal lattice is then forced into a severely distorted state with high elastic strain and hence unusually high stored energy. This energy elevation eventually pushes the crystal to above the energy state of the amorphous phase, triggering the instability of the lattice, which then collapses into the amorphous state. These observations, validated by extensive previous research regarding the formation of amorphous metals [3,7], confirm that most metals can be amorphized, albeit the amorphous state is reached through different pathways. Elemental FCC metals are arguably the most difficult to be rendered amorphous, but the latter state can nevertheless be accessed when the local volume is under external mechanical forcing when other alternative deformation/transformation routes are forbidden.

Declaration of Competing Interest

The authors declare that they have no known competing financial interests or personal relationships that could have appeared to influence the work reported in this paper.

Acknowledgments

This work was supported by the [Beijing Natural Science Foundation \(Z180014\)](#) and the Beijing Outstanding Young Scientists Projects (BJJWZYJH01201910005018), the [Natural Science Foundation of China \(12174014, 91860202\)](#) and "111" project (DB18015). E.M. acknowledges XJTU for hosting his work at CAID.

References

- [1] W. Klement, R.H. Willens, P. Duwez, *Nature* 187 (1960) 869–870.
- [2] L.A. Greer, *Science* 267 (1995) 1947–1953.
- [3] W.L. Johnson, *Mater. Sci. Forum* 225–227 (1996) 35–50 <https://doi.org/10.4028/www.scientific.net/MSF.225-227.35>.
- [4] S.Y. Ding, Y.H. Liu, Y.L. Li, Z. Liu, S.W. Sohn, F.J. Walker, J. Schroers *Nat. Mater.* 13 (2014) 494–500.
- [5] H.A. Davies, J. Aucote, J.B. Hull, *Nature* 246 (1973) 13–14.
- [6] C.-J. Lin, F. Spaepen, *Appl. Phys. Lett.* 41 (1982) 721–723.
- [7] W.L. Johnson, *Prog. Mater. Sci.* 30 (1986) 81–134.
- [8] L. Zhong, J.W. Wang, H.W. Sheng, Z. Zhang, S.X. Mao, *Nature* 512 (2014) 177–180.
- [9] D. Turnbull, *Contemp. Phys.* 10 (1969) 473–488.
- [10] M.H. Bhat, V. Molinero, E. Soignard, V.C. Solomon, S. Sastry, J.L. Yarger, C.A. Angell, *Nature* 448 (2007) 787–790.
- [11] S. Han, L. Zhao, Q. Jiang, J.S. Lian, *Sci. Rep.* 2 (2012) 493 UK.
- [12] X.X. Shen, Z. Xu, J.S. Lian, Q. Jiang, *Mater. Sci. Eng. A* 528 (2011) 7878–7886.
- [13] X.Z. Liao, Y.H. Zhao, Y.T. Zhu, R.Z. Valiev, D.V. Gunderov, *J. Appl. Phys.* 96 (2004) 636–640.
- [14] H. Wang, D.K. Chen, X.H. An, Y. Zhang, S.J. Sun, Y.Z. Tian, Z.F. Zhang, A.G. Wang, J.Q. Liu, M. Song, S.P. Ringer, T. Zhu, X.Z. Liao, *Sci. Adv.* 7 (2021) eabe3105.
- [15] L.H. Wang, J. Teng, X.C. Sha, J. Zou, Z. Zhang, X.D. Han, *Nano Lett.* 17 (2017) 4733–4739.
- [16] S.D. Sun, D.W. Li, C.P. Yang, L.B. Fu, D.L. Kong, Y. Lu, Y.Z. Guo, D.M. Liu, P.F. Guan, Z. Zhang, J.H. Chen, W.Q. Ming, L.H. Wang, X.D. Han, *Phys. Rev. Lett.* 128 (2022) 015701.
- [17] L.B. Fu, C.P. Yang, R.J. Wei, X.F. Pei, J. Teng, D.L. Kong, Y. Lu, Y.Z. Guo, T.F. Liu, Y.L. Hu, B.C. Yin, Z. Zhang, A. Li, L.H. Wang, X.D. Han, *Mater. Today Nano* 15 (2021) 100123.
- [18] M.J. Hÿtch, E. Snoeck, R. Kilaas, *Ultramicroscopy* 74 (1998) 131–146.
- [19] J.L. Taraci, M.J. Hÿtch, T. Clement, P. Peralta, M. McCartney, J. Drucker, S.T. Picraux, *Nanotechnology* 16 (2005) 2365–2371.
- [20] R. Komanduri, N. Chandrasekaran, L.M. Raff, *Int. J. Mech. Sci.* 43 (2001) 2237–2260.